LETTER

doi:10.1038/nature23022

Quantum simulation of a Fermi–Hubbard model using a semiconductor quantum dot array

T. Hensgens[1], T. Fujita[1], L. Janssen[1], Xiao Li[2], C. J. Van Diepen[3], C. Reichl[4], W. Wegscheider[4], S. Das Sarma[2] & L. M. K. Vandersypen[1]

Interacting fermions on a lattice can develop strong quantum correlations, which are the cause of the classical intractability of many exotic phases of matter[1–3]. Current efforts are directed towards the control of artificial quantum systems that can be made to emulate the underlying Fermi–Hubbard models[4–6]. Electrostatically confined conduction-band electrons define interacting quantum coherent spin and charge degrees of freedom that allow all-electrical initialization of low-entropy states and readily adhere to the Fermi–Hubbard Hamiltonian[7–17]. Until now, however, the substantial electrostatic disorder of the solid state has meant that only a few attempts at emulating Fermi–Hubbard physics on solid-state platforms have been made[18,19]. Here we show that for gate-defined quantum dots this disorder can be suppressed in a controlled manner. Using a semi-automated and scalable set of experimental tools, we homogeneously and independently set up the electron filling and nearest-neighbour tunnel coupling in a semiconductor quantum dot array so as to simulate a Fermi–Hubbard system. With this set-up, we realize a detailed characterization of the collective Coulomb blockade transition[20], which is the finite-size analogue of the interaction-driven Mott metal-to-insulator transition[1]. As automation and device fabrication of semiconductor quantum dots continue to improve, the ideas presented here will enable the investigation of the physics of ever more complex many-body states using quantum dots.

The potential for realizing novel electronic and magnetic properties of correlated-electron phases in low-dimensional condensed-matter physics, in fields ranging from high-T_c superconductivity to electronic spin liquids[1–3], has prompted quantum simulation efforts across multiple platforms[4–6,18,19,21,22]. Theoretical and proof-of-principle experimental work has shown how emergent spin physics[21] and two-site Mott physics[22] can be simulated on programmable quantum computing platforms. These digital quantum simulation efforts promise universality, but come at the cost of requiring large numbers of highly controlled quantum bits with additional error-correction overhead. Analogue quantum simulation efforts, on the other hand, aim to implement well-defined Hamiltonians directly. Such emulators are typically limited by the residual entropy of the initialized system, restricting experimental correlations in span and strength[6]. Furthermore, scaling to sufficiently homogeneous systems of larger size is not always straightforward[4–6,19].

Semiconductor quantum dots form a scalable platform that is naturally described by a Fermi–Hubbard model in the low-temperature, strong-interaction regime, when cooled down to dilution temperatures[7–10]. As such, pure state initialization of highly entangled states is possible even without the use of adiabatic initialization schemes[23]. Coherent evolution of excitations can span many sites, as, contrary to what might be expected, more than 20 coherent oscillations in charge or spin can be observed on adjacent sites[13–15]. Furthermore, local control and read-out of both charge and spin degrees of freedom have become mature areas of research, given the large ongoing effort towards using quantum dots as a platform for quantum information processing[11–17]. In particular, excellent control of small on-site energy differences[24] or tunnel couplings[14,15] has been shown at specific values of electron filling and tuning.

Quantum simulation experiments can make use of many of these developments, trading off some of the experimental difficulties involved in full coherent control for ease of scaling. Until now, however, calibration routines for quantum dots have been quite inefficient and limited in scope. As such, the effective control of larger parameter spaces as well as the calibration of larger samples seem like insurmountable obstacles. What has been lacking, therefore, is an efficient and scalable control paradigm for Hamiltonian engineering that extends to the collective Fermi–Hubbard parameter regimes well beyond those required for qubit operation[25,26].

In this Letter, we demonstrate the simulation of Fermi–Hubbard physics using semiconductor quantum dots. We describe an experimental toolbox, validated by direct numerical simulations, that allows for the independent tuning of filling and tunnel coupling as well as the measurement of all interaction energies, and use it to map out the accessible parameter space of a triple-quantum-dot device with unprecedented detail and precision. As the tunnel couplings are homogeneously increased, we witness the delocalization transition between isolated Coulomb blockade and collective Coulomb blockade, the finite-size analogue of the interaction-driven Mott transition.

The one-dimensional quantum dot array is electrostatically defined using voltages applied to gate electrodes fabricated on the surface of a GaAs/AlGaAs heterostructure (Fig. 1) that selectively deplete regions of the 85-nm-deep two-dimensional electron gas (2DEG) underneath. The outermost dots can be (un)loaded from adjacent Fermi reservoirs, which have an effective electron temperature of 70–75 mK (6.0–6.5 μeV). The three gates at the top are used to define a sensing-dot channel, the conductance of which is sensitive to changes in the charge state of the array and is directly read out using radio-frequency reflectometry.

The control of Fermi–Hubbard model parameters is achieved by modulation of the potential landscape in the 2DEG using the seven bottom-most gate electrodes (Fig. 1). These gates come in two types. Plunger gates P_i are designed to tune the single-particle energy offsets ϵ_i of individual dots i, allowing us to set an overall chemical potential $\mu' = \langle \epsilon_i \rangle$ and add site-specific detuning terms $\delta\epsilon_i$. Barrier gates B_{ij} allow for the modulation of tunnel couplings t_{ij} between the ith and jth dot or of Γ_i between an outer dot i and its adjacent Fermi reservoir. The interaction energies are determined by the potential landscape realized to achieve this set $\{\mu', \delta\epsilon_i, t_{ij}, \Gamma_i\}$, and comprise the on-site Coulomb interaction terms U_i and the inter-site Coulomb interaction terms V_{ij}. With each dot filled with an even number of electrons, we can describe the addition of the next two electrons per dot within an effective

[1]QuTech and Kavli Institute of Nanoscience, TU Delft, 2600 GA Delft, The Netherlands. [2]Condensed Matter Theory Center and Joint Quantum Institute, University of Maryland, College Park, Maryland 20742, USA. [3]QuTech and Netherlands Organization for Applied Scientific Research (TNO), 2600 AD Delft, The Netherlands. [4]Solid State Physics Laboratory, ETH Zürich, 8093 Zürich, Switzerland.

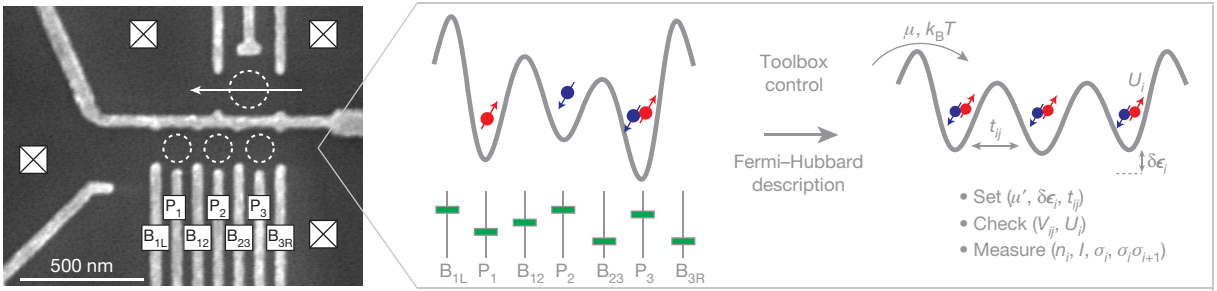

Figure 1 | Gate-defined quantum dot array as a platform for quantum simulations of the Fermi–Hubbard model. Left, electron micrograph of a sample nominally identical to the one used for the measurements. The bottom three dashed circles indicate the triple-quantum-dot array, whose Hamiltonian parameters derive from the local potential landscape controlled by the seven gates under (B_{1L} to B_{3R}). The top dashed circle and arrow indicate the sensing dot channel, the radio-frequency reflectance of which is monitored to enable real-time charge sensing. Crossed squares indicate distinct Fermi reservoirs that are contacted using ohmic contacts. Right, diagrams showing how setting the gates controls the potential landscape, filled with a given number of spin-up (red) and spin-down (blue) electrons and how a Fermi–Hubbard model is set up. We describe a toolbox that allows for the control of the quantum dot array at the level of the microscopic Fermi–Hubbard model. In particular, it allows for the independent calibration of $\{\mu', \delta\epsilon_i, t_{ij}\}$ and the measurement of the Coulomb interaction terms $\{V_{ij}, U_i\}$ (see Fig. 2, main text and Methods). Measurable observables for quantum dots include both local charge occupation and global charge transport as well as local spin degrees of freedom and nearest-neighbour singlet–triplet spin correlations (through spin-to-charge conversion protocols[11,16,17]).

single-band extended Hubbard picture[27], using site-and-spin-specific electronic creation and annihilation operators $c_{i\sigma}^{\dagger}$ and $c_{i\sigma}$, and dot occupations $n_i = \sum_\sigma c_{i\sigma}^{\dagger} c_{i\sigma}$ (h.c. below indicates Hermitian conjugate):

$$H = -\sum_i \epsilon_i n_i - \sum_{<i,j>,\sigma} t_{ij}(c_{i\sigma}^{\dagger} c_{j\sigma} + \text{h.c.}) + \sum_i \frac{U_i}{2} n_i(n_i - 1) + \sum_{i,j} V_{ij} n_i n_j \quad (1)$$

In practice, both P_i and B_{ij} gates exhibit cross-talk to all the ϵ_i, Γ_i and t_{ij} (with smaller effects on U_i and V_{ij}), and in addition must compensate for initial disorder. Setting Hamiltonian parameters experimentally therefore requires carefully chosen linear combinations of gate voltages. This idea is employed regularly in spin qubit experiments in order to change the on-site energies ϵ_i deterministically over small ranges[24], but here we go further in important ways. Our experimental toolbox uses linear combinations of gate voltage changes $\{P_i, B_{ij}\}$ for the independent control of the Fermi–Hubbard parameters $\{\mu', \delta\epsilon_i, t_{ij}\}$ to within several $k_B T$ and over a wide range of fillings and tunnel couplings.

Figure 2a, b shows the filling of the array with up to $N = 9$ electrons, three electrons per dot, while keeping the inter-dot tunnelling terms small ($t_{ij} < V_{ij} < U_i$) and the tunnel couplings to the reservoirs roughly constant. The dark lines arise from steps in the charge detector conductance, indicating a transition in the number of electrons on one of the dots. The horizontal and diagonal lines indicate filling of one of the dots from the reservoir, whereas the vertical (polarization) lines indicate electron transitions between sites (not seen in Fig. 2b, which shows only changes in N). To achieve this level of control required several new insights. As a start, we measure the cross-talk between the seven gate voltages and the three dot detunings at multiple points in gate space, allowing for the direct definition of virtual $\delta\epsilon_i$ gates that are accurate over a range of several meV (see Methods and Extended Data Fig. 1). Furthermore, it allows us to define virtual barrier gates that change specific tunnel couplings while keeping all dot detunings constant. In addition, we achieve homogeneous filling of a quantum dot array (as in Fig. 2a) through non-homogeneous changes in the ϵ_i, as the dots have to each overcome a different sum of local interaction energies $U_i + \sum_{i \neq j} V_{ij}$. This is a consequence of the finite size of the array (only the middle dot has two neighbours) and the inhomogeneity in interaction terms (see Methods and Extended Data Figs 2, 3). Finally, as multiple electrons are added to the array, we use the virtual barrier gates described above to counter the effect that changing plunger gate voltages (and the higher wavefunction overlap of higher electron fillings) have on the tunnel couplings.

Having filled the array with a given number of electrons, we can quantitatively characterize the various parameters in the Fermi–Hubbard model directly from relevant feature sizes in the charge stability diagram as we detune away from uniform filling. The spacing between charge addition lines of half-filled dot levels yields the on-site Coulomb interaction term U_i, whereas the displacement of single charge addition lines on filling with another dot yields their inter-site Coulomb coupling V_{ij} (see Fig. 2c and Methods for automation and protocols). Finally, we can extract the inter-dot tunnel coupling t_{ij} at transitions where an added electron moves between adjacent sites i and j (the polarization lines seen in Fig. 2a). The width of such transitions is determined by the hybridization of the charge states on the two sites and is thus a measure of tunnel coupling. We implement an iterative tuning process that allows for automated repeated measurements at rates of 1 Hz of the polarization line width with changing virtual barrier gates and thus tunnel coupling. To account for the only remaining cross-talk, that between each virtual barrier gate and the other tunnel coupling, we redefine the virtual barrier gates such that they influence their local tunnel coupling only, while keeping all other parameters constant (see Fig. 2d and Extended Data Fig. 4).

We demonstrate the potential of well-controlled quantum dot arrays to emulate Fermi–Hubbard physics by employing this newly developed toolbox for the realization of collective Coulomb blockade physics, validating the results through direct numerical Fermi–Hubbard model calculations. Coulomb blockade is a purely classical effect that arises from the finite charging energies of each individual quantum dot, where a gap for charge excitations exists at half filling, analogous to the Mott gap. When quantum tunnelling effects between sites are turned on, however, a much richer phase diagram appears. The Coulomb blockade of individual dots is destroyed as the degeneracy of the peaks in the equilibrium charge addition spectrum is lifted and broadened into minibands, giving way to collective Coulomb blockade[20] (see Fig. 3a and Extended Data Fig. 5 for simulated data of a simplified model). As tunnel couplings continue to increase relative to local charging energies, the gap for charge excitations will vanish in the thermodynamic limit, giving rise to a metallic state. The physics of collective Coulomb blockade is best described by the equilibrium electron addition spectrum as a function of filling and tunnel coupling, which are the two main experimental control parameters of the quantum dot array.

The experimental phase diagram is mapped out by independent control over electron filling and tunnel coupling strength over as large a range as possible (Methods). It is constructed continuously by linear interpolation of gate values between 3–12 calibrated points per miniband (Fig. 3b) where the on-site energies and tunnel couplings are well calibrated and the interaction energies measured (see

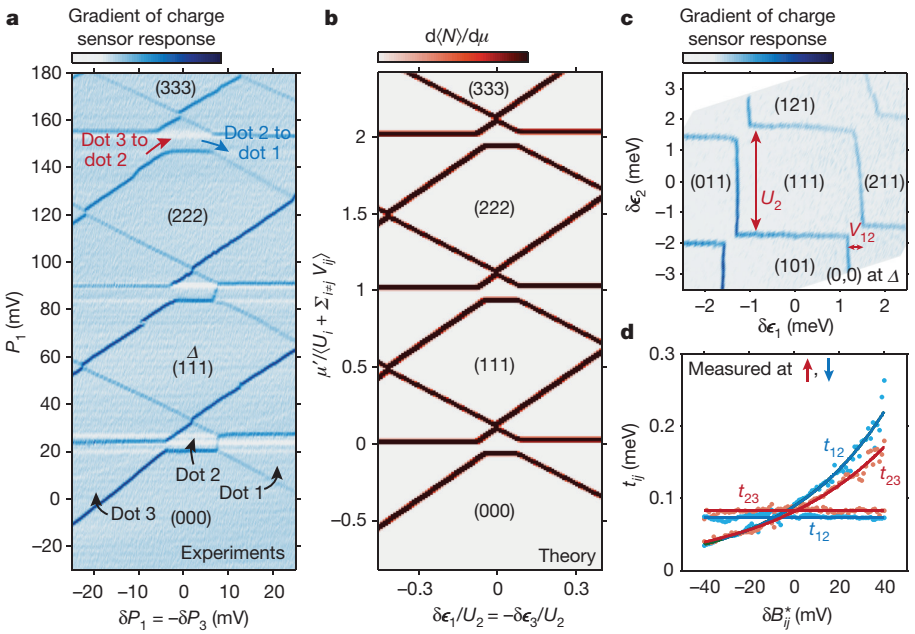

Figure 2 | Hamiltonian engineering using a scalable toolbox of local control and measurements. a, Charge stability diagram showing uniform filling of the array of up to three electrons per dot in the vertical direction, using a combination of all seven gate voltages (only P_1 values are shown) that equally sweeps the local fillings n_i while keeping the tunnel couplings between dots and to the reservoirs nominally identical. Lines correspond to charge transitions. Δ indicates the centre of the measurements of **c**, whereas the blue and red arrows indicate respectively the transitions where the measurements of t_{12} and t_{23} of **d** were performed. **b**, Theoretical charge stability diagram of a triple-quantum-dot system in the classical limit ($t = 0$) exchanging particles with a reservoir at $k_BT/U = 0.003$, showing the addition of electrons as a function of homogeneous filling (vertical) and detuning of the outer dots (horizontal), analogous to the measurement in **a**. **c**, As we focus on relevant sections of the charge-stability diagram of the array, we calibrate all relative cross-capacitances of the seven-gate, three dot-system, allowing for deterministic changes in ϵ_i and subsequent measurement of on-site and inter-site Coulomb couplings. U_2 and V_{12} are shown as examples. **d**, Measurements of both tunnel couplings as a function of two linear combinations of gate voltages, B^*_{12} and B^*_{23}, that keep either t_{23} or t_{12} (the full line denotes the average value) as well as the three on-site energies ϵ_i constant while increasing t_{12} or t_{23}, respectively (an exponential fit to $\alpha\exp(B^*_{ij}/\beta)$ is shown). Individual tunnel coupling data points for t_{12} and t_{23} are taken at the transitions indicated by the blue and red arrow in **a** and have typical fitting errors of several per cent (not shown). Text in brackets denote the dominant charge states in the many-body eigenstate.

Extended Data Fig. 6). At low tunnel coupling, the miniband has a finite width owing to residual V_{ij}. The main effect of increased nearest-neighbour tunnel coupling on the addition spectrum is a widening of the minibands at the expense of the collective gap at uniform filling, analogous to the reduction of the Mott gap with increasing tunnel coupling. Along with tunnel coupling, the inter-site Coulomb coupling V_{ij} also increases (see Extended Data Fig. 6). The gap between minibands continues to decrease with increasing tunnel coupling, but will be prohibited from closing completely by the charging energy of what has essentially become one large dot: this energy is inversely proportional to the large but finite total capacitance of the 'large dot'. The low and high tunnel coupling regimes are also clearly distinguished

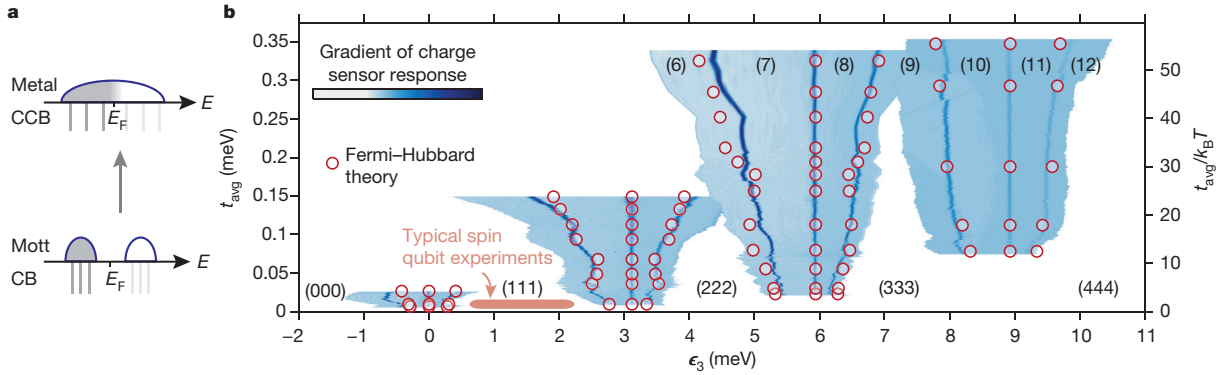

Figure 3 | Collective Coulomb blockade physics in the Fermi–Hubbard phase space. a, Schematic representation of the charge addition spectrum of a Mott insulator at half filling and a triple-quantum-dot array in Coulomb blockade (CB: bottom) and those of a metallic phase at half filling and a triple-quantum-dot array in collective Coulomb blockade (CCB: top). **b**, The experimentally accessible parameter space of the Fermi–Hubbard model for a triple-quantum-dot array as a function of electron filling and nearest-neighbour tunnel coupling. Continuous charge sensing measurements following the charging lines are shown, at calibrated gate values where the dots are filled homogeneously (only ϵ_3 values are shown) and the values of t_{ij} are set to be roughly equal. Plotted spacings between the bands are set by the Coulomb interaction terms measured at small tunnel coupling. Red circles indicate extended Hubbard model calculations of the transitions. In the vertical direction, they are set using the same measured $t_{avg} = (t_{12} + t_{23})/2$ as the experimental data. In the horizontal direction, the simulations start from measured interaction energies with about 10% errors (see Methods, Extended Data Fig. 6 and Extended Data Tables 1, 2). Text in brackets denotes electron filling, red shading indicates the section of the experimental phase space that is typically accessed in spin qubit experiments.

in transport measurements through the quantum dot array and in charge stability diagrams (see Extended Data Fig. 7). To test the validity of our approach, we perform numerical calculations of the addition spectrum within each band based on equation (1) and using experimental parameters that are either calibrated or measured (see Methods and Extended Data Tables 1, 2). The agreement between measurement and numerical calculation in Fig. 3b indeed validates the experimental tools for Hamiltonian engineering over the entire measured diagram.

Putting these results in perspective, we are able to calibrate and characterize site-specific quantum dot parameters up to values of tunnel coupling reaching $U/t = 7.1(4)$. The large energy scales obtained compared to temperature, $t/k_BT = 54(5)$, give access to the regime where quantum correlations are strong[1–3]. Extending this work to larger quantum dot arrays, whether for the purpose of analogue quantum simulation or quantum computation, requires further automation of our methods[28], and extensions to parallelize the calibration routines. Scalable gate layouts for one-dimensional arrays already exist[29], which, together with the programmable disorders in on-site energies, can be mapped onto the physics of many-body localization[30]. Further advances in connectivity and homogeneity are underway in the pursuit of scalable quantum computing—including square[31] and triangular[32] geometries, industrial-grade fabrication processes and magnetically quiet ^{28}Si substrates[33]—and open up further possibilities for quantum simulation experiments with quantum dots.

Online Content Methods, along with any additional Extended Data display items and Source Data, are available in the online version of the paper; references unique to these sections appear only in the online paper.

Received 13 February; accepted 12 June 2017.

1. Imada, M., Fujimori, A. & Tokura, Y. Metal-insulator transitions. *Rev. Mod. Phys.* **70,** 1039–1263 (1998).
2. Balents, L. Spin liquids in frustrated magnets. *Nature* **464,** 199–208 (2010).
3. Anderson, P. W. Twenty-five years of high-temperature superconductivity — a personal review. *J. Phys. Conf. Ser.* **449,** 012001 (2013).
4. Jördens, R., Strohmaier, N., Günter, K., Moritz, H. & Esslinger, T. A Mott insulator of fermionic atoms in an optical lattice. *Nature* **455,** 204–207 (2008).
5. Tanese, D. *et al.* Polariton condensation in solitonic gap states in a one-dimensional periodic potential. *Nat. Commun.* **4,** 1749 (2013).
6. Mazurenko, A. *et al.* A cold-atom Fermi–Hubbard antiferromagnet. *Nature* **545,** 462–466 (2017).
7. Manousakis, E. A quantum-dot array as model for copper-oxide superconductors: a dedicated quantum simulator for the many-fermion problem. *J. Low Temp. Phys.* **126,** 1501–1513 (2002).
8. Byrnes, T., Kim, N. Y., Kusudo, K. & Yamamoto, Y. Quantum simulation of Fermi-Hubbard models in semiconductor quantum-dot arrays. *Phys. Rev. B* **78,** 075320 (2008).
9. Yang, S., Wang, X. & Das Sarma, S. Generic Hubbard model description of semiconductor quantum-dot spin qubits. *Phys. Rev. B* **83,** 161301 (2011).
10. Barthelemy, P. & Vandersypen, L. M. K. Quantum dot systems: a versatile platform for quantum simulations. *Ann. Phys.* **525,** 808–826 (2013).
11. Petta, J. R. *et al.* Coherent manipulation of coupled electron spins in semiconductor quantum dots. *Science* **309,** 2180–2184 (2005).
12. Koppens, F. H. L. *et al.* Driven coherent oscillations of a single electron spin in a quantum dot. *Nature* **442,** 766–771 (2006).
13. Petersson, K. D., Petta, J. R., Lu, H. & Gossard, A. C. Quantum coherence in a one-electron semiconductor charge qubit. *Phys. Rev. Lett.* **105,** 246804 (2010).
14. Martins, F. *et al.* Noise suppression using symmetric exchange gates in spin qubits. *Phys. Rev. Lett.* **116,** 116801 (2016).
15. Reed, M. D. *et al.* Reduced sensitivity to charge noise in semiconductor spin qubits via symmetric operation. *Phys. Rev. Lett.* **116,** 110402 (2016).
16. Baart, T. A. *et al.* Single-spin CCD. *Nat. Nanotechnol.* **11,** 330–334 (2016).
17. Gray, J., Bayat, A., Puddy, R. K., Smith, C. G. & Bose, S. Unravelling quantum dot array simulators via singlet-triplet measurements. *Phys. Rev. B* **94,** 195136 (2016).
18. Singha, A. *et al.* Two-dimensional Mott-Hubbard electrons in an artificial honeycomb lattice. *Science* **332,** 1176–1179 (2011).
19. Salfi, J. *et al.* Quantum simulation of the Hubbard model with dopant atoms in silicon. *Nat. Commun.* **7,** 11342 (2016).
20. Stafford, C. A. & Das Sarma, S. Collective Coulomb blockade in an array of quantum dots: a Mott-Hubbard approach. *Phys. Rev. Lett.* **72,** 3590–3593 (1994).
21. Lanyon, B. P. *et al.* Universal digital quantum simulation with trapped ions. *Science* **334,** 57–61 (2011).
22. Barends, R. *et al.* Digital quantum simulation of fermionic models with a superconducting circuit. *Nat. Commun.* **6,** 7654 (2015).
23. Farooq, U., Bayat, A., Mancini, S. & Bose, S. Adiabatic many-body state preparation and information transfer in quantum dot arrays. *Phys. Rev. B* **91,** 134303 (2015).
24. Oosterkamp, T. H. *et al.* Microwave spectroscopy of a quantum-dot molecule. *Nature* **395,** 873–876 (1998).
25. Livermore, C. *et al.* The Coulomb blockade in coupled quantum dots. *Science* **274,** 1332–1335 (1996).
26. Lee, S. D. *et al.* Single-electron spectroscopy in a triple-dot system: role of interdot electron-electron interactions. *Phys. Rev. B* **62,** R7735–R7738 (2000).
27. Wang, X., Yang, S. & Das Sarma, S. Quantum theory of the charge-stability diagram of semiconductor double-quantum-dot systems. *Phys. Rev. B* **84,** 115301 (2011).
28. Baart, T. A., Eendebak, P. T., Reichl, C., Wegscheider, W. & Vandersypen, L. M. K. Computer-automated tuning of semiconductor double quantum dots into the single-electron regime. *Appl. Phys. Lett.* **108,** 213104 (2016).
29. Medford, J. *et al.* Self-consistent measurement and state tomography of an exchange-only spin qubit. *Nat. Nanotechnol.* **8,** 654–659 (2013).
30. Basko, D. M., Aleiner, I. L. & Altshuler, B. L. Metal-insulator transition in a weakly interacting many-electron system with localized single-particle states. *Ann. Phys.* **321,** 1126–1205 (2006).
31. Thalineau, R. *et al.* A few-electron quadruple quantum dot in a closed loop. *Appl. Phys. Lett.* **101,** 103102 (2012).
32. Seo, M. *et al.* Charge frustration in a triangular triple quantum dot. *Phys. Rev. Lett.* **110,** 046803 (2013).
33. Veldhorst, M. *et al.* An addressable quantum dot qubit with fault-tolerant control-fidelity. *Nat. Nanotechnol.* **9,** 981–985 (2014).

Acknowledgements We acknowledge discussions with M. Veldhorst, A. F. Otte, R. Sensarma and the members of the Vandersypen group, sample fabrication by F. R. Braakman, set-up preparation by T. A. Baart and experimental assistance from M. Ammerlaan, J. Haanstra, R. Roeleveld, R. Schouten and R. Vermeulen. This work was supported by the Netherlands Organization of Scientific Research (NWO) VICI programme, the European Commission via the integrated project SIQS, the Japan Society for the Promotion of Science (JSPS) Postdoctoral Fellowship for Research Abroad, LPS-MPO-CMTC and the Swiss National Science Foundation.

Author Contributions T.H., T.F., C.J.v.D. and L.J. performed the experiments and analysed the data, C.R. and W.W. grew the heterostructure, X.L. and S.D.S. performed the theoretical analyses with X.L. carrying out the numerical simulations, T.H., T.F., X.L., L.J., S.D.S. and L.M.K.V. contributed to the interpretation of the data, and T.H. wrote the manuscript (X.L. wrote part of the Methods), with comments from T.F., X.L., S.D.S. and L.M.K.V.

Author Information Reprints and permissions information is available at www.nature.com/reprints. The authors declare no competing financial interests. Readers are welcome to comment on the online version of the paper. Publisher's note: Springer Nature remains neutral with regard to jurisdictional claims in published maps and institutional affiliations. Correspondence and requests for materials should be addressed to L.M.K.V. (l.m.k.vandersypen@tudelft.nl).

Reviewer Information *Nature* thanks S. Bose, S. Rogge, J. Salfi and the other anonymous reviewer(s) for their contribution to the peer review of this work.

METHODS

Materials and set-up. The triple-quantum-dot sample was fabricated on a GaAs/$Al_{0.25}Ga_{0.75}As$ heterostructure that was grown by molecular-beam epitaxy. The 85-nm-deep 2D electron gas has an electron density of $2.0 \times 10^{11}\,cm^{-2}$ and 4 K mobility of $5.6 \times 10^{6}\,cm^{2}\,V^{-1}\,s^{-1}$. All sample structures were defined using electron-beam lithography, with metallic gates (Ti/Au) and ohmic contacts (Ni/AuGe/Ni) deposited on the bare wafer in a lift-off process using electron-beam evaporation, similarly to the definition of metallic markers, leads and bonding pads, and with sample mesas defined using a diluted Piranha wet etch. The plunger gates were connected to bias-tees on the printed circuit board, allowing fast sweeps and RF excitations to be applied in addition to DC voltages. RF reflectometry[34] of the sensing dot channel conductance is done at 110.35 MHz employing a homebuilt *LC* circuit on the printed circuit board. The sample was cooled down in an Oxford Kelvinox 400HA dilution refrigerator to a base temperature of 45 mK while applying positive bias voltages to all gates. With the sample cold and the dots formed through application of appropriate voltages to the metallic gates, read-out was performed by feeding the RF reflectometry circuit a roughly −99 dBm carrier wave, the reflected signal of which is amplified at 4 K and subsequently demodulated and measured using custom electronics. Using this technique on a sensing dot is preferred to forming a quantum point contact, and yields measurement bandwidths exceeding 1 MHz. The sensing dot position is asymmetric in order to obtain different sensitivities to each of the three dots. Note that as an alternative to electrostatically defined charge sensors in the 2DEG itself, dispersive read-out using the nanofabricated top gates would allow measurement of how much charges move in response to gate voltage changes[35]. For more detailed methods, please see ref. 16.

Eliminating cross-talk through the definition of virtual gates. Changes in ϵ_i can be tracked directly by following transitions in the charge stability diagram and are found to depend linearly on gate values for voltage changes up to several tens of millivolts. In general, small changes in the energy offsets of each of the three dots will thus be achieved via a linear combination of voltage changes on each of the seven gates:

$$\delta\begin{pmatrix}\epsilon_1\\ \epsilon_2\\ \epsilon_3\end{pmatrix}=\begin{pmatrix}\alpha_{11} & \alpha_{12} & \alpha_{13} & \alpha_{14} & \alpha_{15} & \alpha_{16} & \alpha_{17}\\ \alpha_{21} & \alpha_{22} & \alpha_{23} & \alpha_{24} & \alpha_{25} & \alpha_{26} & \alpha_{27}\\ \alpha_{31} & \alpha_{31} & \alpha_{33} & \alpha_{34} & \alpha_{35} & \alpha_{36} & \alpha_{37}\end{pmatrix}\delta(P_1\ P_2\ P_3\ B_{1L}\ B_{12}\ B_{23}\ B_{3R})^{T}.$$

Of these 21 matrix elements, the three α_{ii}s describe the coupling of the plungers P_i to the energy offset ϵ_i of their respective dot *i*. The other 18 elements are cross-talks, whose values can easily be related to the α_{ii}s through the slope of charge addition lines (see Extended Data Fig. 1a). This leaves the relative weights of the α_{ii}s and the absolute value of one of the elements to be determined. As the difference between the single-particle energies of two dots stays fixed along a polarization line, we can determine the relative weights from the slope of these lines (see Extended Data Fig. 1b). The absolute value of α_{22} is called the lever arm and can be found using photon-assisted tunnelling measurements (see Extended Data Fig. 4). For the measurements presented in Fig. 3b, the matrix has been measured multiple times for different fillings and tunnel couplings: the 'plunger' side α_{11}–α_{33} of the matrix was measured 25 times in total and the 'barrier' part α_{14}–α_{37} 12 times (see Extended Data Fig. 1c). In between these points, we used linear interpolation as a function of measured tunnel coupling to extract matrix elements when needed.

With all matrix elements known, the ϵ_is can be deterministically changed, a technique which is extensively used throughout the results presented here in two main ways: (1) by measuring Hamiltonian parameters through direct interpretation of features in the addition spectrum; and (2) through the definition of 'virtual gates', both for plunger and barrier gates, that greatly simplify the tuning process. For instance, the virtual gate for the energy offset of the leftmost dot, ϵ_1, is defined by a simple combination of plunger gates: $\delta\begin{pmatrix}P_1\\ P_2\\ P_3\end{pmatrix}=\begin{pmatrix}\alpha_{11} & \alpha_{12} & \alpha_{13}\\ \alpha_{21} & \alpha_{22} & \alpha_{23}\\ \alpha_{31} & \alpha_{32} & \alpha_{33}\end{pmatrix}^{-1}\begin{pmatrix}\delta\epsilon_1\\ 0\\ 0\end{pmatrix}$. To form virtual barrier gates we use $\delta B_{12}\rightarrow\delta B'_{12}=\delta(P_1,P_2,P_3,B_{12})$ with $\delta\begin{pmatrix}P_1\\ P_2\\ P_3\end{pmatrix}=-\delta B_{12}\begin{pmatrix}\alpha_{11} & \alpha_{12} & \alpha_{13}\\ \alpha_{21} & \alpha_{22} & \alpha_{23}\\ \alpha_{31} & \alpha_{32} & \alpha_{33}\end{pmatrix}^{-1}\begin{pmatrix}\alpha_{14}\\ \alpha_{24}\\ \alpha_{34}\end{pmatrix}$, which allows us to make the barrier separating dots 1 and 2 more (or less) transparent without changing the energy offsets ϵ_i of any of the dots: that is, they stay at the same location in the charge stability diagram. Finally, linear combinations of B'_{12} and its equivalent between dots 2 and 3, B'_{23}, yield the two orthogonal control gates B^{*}_{ij} for changing t_{ij}, as used in Fig. 2d.

Classically coupled dots and homogeneous filling. Isolated quantum dots are well described by a classical capacitance model[36]. This description is valid as long as tunnel coupling energies are negligible compared to capacitive (Coulomb) effects. In this case, the charge states *s* of the system are simply described by the set of individual dot occupations $(n_1, n_2, ...)$ as the n_is are good quantum numbers. As has been shown previously[9], one can map the classical capacitance model onto the extended Hubbard model of equation (1) with omission of its tunnelling terms, which is readily diagonalized with eigenenergies $E(n_1,n_2,...)=-\sum_i\epsilon_i n_i+\sum_i\frac{U_i}{2}n_i(n_i-1)+\sum_{i,j\neq i}V_{ij}n_i n_j$. Because we experimentally probe changes in the equilibrium charge state of the array coupled to adjacent electron reservoirs, which are typically kept at an equal and constant electrochemical potential μ and temperature k_BT, we are interested in the charge addition spectrum $\frac{\partial\langle N\rangle}{\partial\mu}$, with $\langle N\rangle=k_BT\frac{\partial\ln\mathcal{Z}}{\partial\mu}$, $\mathcal{Z}=\mathrm{Tr}\{\exp[-(H-\mu N)/k_BT]\}$, where $N=\sum_i n_i$ is the total electron number and $\mathcal{Z}$ is the grand partition function. In this classical case and at constant chemical potential $\mu=0$, the equations for the charge addition spectrum $\frac{\partial\langle N\rangle}{\partial\mu}=\frac{\langle N^2\rangle-\langle N\rangle^2}{k_BT}$ simplify to simple Boltzmann-weighted sums over the charge states *s*, namely $\mathcal{Z}=\sum_s\exp[-E_s/k_BT]$ and $\langle N^k\rangle=\frac{1}{\mathcal{Z}}\sum_s N_s^k\exp[-E_s/k_BT]$. Note that for the purpose of finding the charge transitions, any spin-degeneracy of the charge states can be ignored. The charge stability measurements shown in the main text effectively show two-dimensional slices of the charge addition spectrum as a function of changes in the ϵ_is.

The filling of the quantum dot array is controlled experimentally by changing the energy difference between the electronic states at the Fermi level of the reservoir and those of the dot array itself. The former can be changed by applying a bias voltage to the relevant Fermi reservoir, and the latter can be changed by applying voltages to top gates that influence the single-particle energies ϵ_i on the dots. Because the partition function is only sensitive to changes in $H-\mu N$, one can equivalently think about changes in the ϵ_is as influencing the chemical potential directly through $\delta(\mu N)=\delta(\sum_i\epsilon_i n_i)$, which at uniform filling simplifies to $\delta\mu=\langle\delta\epsilon_i\rangle$. This allows a different look at gate control over a quantum dot array with *M* sites. Instead of thinking about *M* different ϵ_is, we can define one global chemical potential term $\mu'=\langle\epsilon_i\rangle$ and $M-1$ energy differences $\delta_i=\epsilon_i-\mu'$, where the latter describe the setting of some (controllable) disorder potential landscape at a fixed chemical potential μ'.

In the case of a large and homogeneous system, changing all ϵ_i equally would uniformly and homogeneously fill all dots in the system. For the triple-quantum-dot sample described in the main text, however, both the finite size (for example, only one of the three dots has two direct neighbours) and inhomogeneous interaction terms (for example, $U_1\neq U_2$) mean a different approach is needed: we have to link up a set of well-defined points in $(\epsilon_1,\epsilon_2,\epsilon_3)$-space. In the case of $V_{ij}=0$, and focusing on the regime from 0 to 2 electrons per site, the only obvious choice would be to identify and align points A (where the eight charge states (000) to (111) are degenerate) and point B (where (111) to (222) are degenerate) (see Extended Data Fig. 2a). These points are lined up by changing the on-site single particle energies by the ratio of their on-site repulsions $\epsilon_i=\mu' U_i/\langle U\rangle$. Analogously, under finite V_{ij}, we use the ratio of the sum of all locally relevant interaction energies $W_i=U_i+\sum_{j\neq i}V_{ij}$ as $\epsilon_i=\mu' W_i/\langle W\rangle$. Note, however, that the inter-site repulsion breaks particle–hole symmetry and moves states with more than one particle added to a homogeneously filled state to higher energy, meaning we can only find points with at most 4 degenerate states. We can align points C (where (000), (100), (010) and (001) are degenerate) and D (where (111), (211), (121) and (112) are degenerate) (see Extended Data Fig. 2b), or we can align points E (where (110), (101), (110) and (111) are degenerate) and F (where (221), (212), (221) and (222) are degenerate) (see Extended Data Fig. 2c), the two of which are particle–hole partners of the same total state.

Defining a miniband as the region in chemical potential where one uniform filling transitions to the next one (the first miniband is thus the transition region between (000) and (111)), it becomes clear that the inter-site Coulomb terms already widen the miniband at zero tunnel coupling. On top of this, too large a deviation in the site-specific energy offsets ϵ_is from the desired values (which amounts to disorder in the dot energies) can also increase the miniband width. This can be seen in Fig. 2a and b as we horizontally move away from the centre line. For changes in $\delta\epsilon_2$, the width remains minimized as long as the $\delta\epsilon_2$ remains in the window between two well-defined points denoted by the crosses and diamonds of Extended Data Fig. 2 (see also Extended Data Fig. 3).

Anti-crossing measurement and fit. Much of the day-to-day work in quantum dot arrays in general and for the measurements described here in particular consists of the interpretation of features in the charge stability diagram. In the case of well isolated dots with localized electrons ($t/U\ll 1$), this essentially boils down to one-dot features (parallel lines) and two-dot features (anti-crossings and associated polarization lines). Indeed, pattern recognition of anti-crossings is the crucial step in the automated initial tuning of double quantum dots[28].

In general, the processing of a charge stability diagram (for example, Fig. 2c) starts with finding charge transitions in the raw sensor dot data using an edge finding algorithm. The results are filtered to only leave edge sections with more than a threshold number of points. Next, we employ a k-means algorithm to

cluster the edges into line sections. Depending on the data, manual input might be needed, either in the selection of relevant clusters or, sometimes, in the case of noisy data, manual selection of points. In determining on-site interaction terms U_i, calculating the orthogonal distance between two parallel lines suffices. In the case of an anti-crossing, we employ a 2D fitting routine in a rotated frame $2\begin{pmatrix} y \\ x \end{pmatrix} = \delta\begin{pmatrix} \epsilon_i + \epsilon_j \\ \epsilon_i - \epsilon_j \end{pmatrix} = \begin{pmatrix} 1 & 1 \\ -1 & 1 \end{pmatrix}\begin{pmatrix} \alpha_{ii} & \alpha_{ij} \\ \alpha_{ji} & \alpha_{jj} \end{pmatrix}\delta\begin{pmatrix} P_i \\ P_j \end{pmatrix}$, simultaneously fitting both branches in a least squares sense to $y - y_0 = \pm\left(V_{ij}/2 + \sqrt{(x - x_0)^2 + t_{ij}^2}\right)$. Fitting parameters are three of the matrix elements (corresponding to the angles of the two dot lines and the polarization line), the two offsets x_0 and y_0 and the two energies V_{ij} and t_{ij}. Both the procedures to find U_i and V_{ij} are limited to $t/U < 0.15$, as around this value for the tunnel coupling there are no straight line sections in the charge addition diagram left where two well-defined localized charge states meet. Further discussion on this can be found with Extended Data Fig. 6.

Practical limits to achievable parameter space. As can be seen in Fig. 3b, there are limits to the achievable parameter space in terms of electron filling and tunnel coupling for the device measured. This is mostly due to the gate layout, which was designed for spin qubit experiments at fillings around one electron per site and tunnel couplings up to several tens of μeV (red shaded area in Fig. 3b). The chosen lithographic separation between the dots does not allow for sufficient wavefunction overlap between singly-occupied sites to achieve much larger tunnel couplings. With multiple electrons per dot, however, the wavefunctions are more extended and much larger tunnel couplings are possible. Here, practical difficulties in compensating for cross-talk make it hard to reach very small tunnel couplings.

Verification of miniband width through Fermi–Hubbard calculations. We perform numerical simulations with two levels of detail. Extended Data Fig. 5 shows the collective Coulomb blockade transition in a simplified model to illustrate the main concepts. Results from a more detailed simulation are overlaid with the experimental data in Fig. 3b. We here elaborate on these two approaches.

In the simplified model calculation, we ignored the inter-site Coulomb interactions $V_{ij}n_in_j$, which will split the peaks in the addition spectrum even at zero tunnel coupling, as discussed above. It is included in the detailed model. Because it is difficult to experimentally fix the absolute chemical potential over large areas of the parameter space due to nonlinearities in the gating effects, the addition spectrum in Fig. 3b was constructed by plotting the middle transition within each miniband as a straight line at fixed ϵ_3, and measuring the chemical potentials of adjacent transitions with respect to those. As we can see from Extended Data Fig. 5b, such an approximation is justified at small t/U (<0.15), although it neglects any change in the interaction terms with increasing tunnel coupling. Furthermore, since the interaction parameters are non-constant over the experimental phase space (Extended Data Fig. 6), the detailed simulations take this into account. Finally, as also discussed above, it requires an inhomogeneous change in the site-specific energy offsets to homogeneously fill the array. In order to allow direct comparison to the experiment, we thus have to take the correct (ϵ_1,ϵ_2,ϵ_3) line to describe the filling (horizontal axis of Fig. 3b). Note that because of the non-constant interaction energies, this vector will generally differ with miniband number and tunnel coupling.

In order to find the correct filling vector and subsequently the position of the transitions, we use the following procedure for each data set at a particular tunnel coupling and miniband number: (i) When the system has $N = 3n$ electrons, its ground state is tuned to be the (n, n, n,) state. (ii) The two critical points (both for n and $n' = n + 1$) at which the four states (n, n, n,), ($n \pm 1$, n, n), (n, $n \pm 1$, n) and (n, n, $n \pm 1$) are degenerate are identified. (iii) Linking these points in the three-dimensional parameter space spanned by (ϵ_1, ϵ_2, ϵ_3) yields the filling line $\delta(\epsilon_1,\epsilon_2,\epsilon_3)$. (iv) The three charge transitions of the miniband are subsequently found to lie somewhere on this line. (v) This procedure yields a fixed width of the miniband, but leaves one degree of freedom unspecified, which is the relative position of the middle dot detuning relative to the outer dots, addressed in the next paragraph.

We illustrate this procedure for the data with the second largest tunnel couplings in the fourth miniband in Fig. 3b in the main text, for which the following set of quantum dot parameters applies: $t = 0.29$, $U_1 = 2.26$, $U_2 = 2.70$, $U_3 = 2.48$, $V_{12} = 0.65$, $V_{23} = 0.57$, $V_{13} = 0.43$ (all in meV). First of all, it is helpful to show the 'uniform' chemical potential μ that correspond to the specific ϵ_is (a 'global' chemical potential μ can be regained through $\mu = \frac{1}{N}\sum_i \epsilon_i n_i$). Such a comparison is shown in Extended Data Table 1. We can see that in the three-dimensional parameter space the filling vector defined by $\delta(\epsilon_1,\epsilon_2,\epsilon_3)$ can be very different from the one defined by $\delta(\mu, \mu, \mu)$. This shows that the distinction is important, and a simple simulation with a uniform chemical potential as in Extended Data Fig. 5b will not compare well with the experiment. Second, we note that the simulations are done for the specific middle dot detuning denoted by the asterisk in Extended Data Fig. 2b and Extended Data Fig. 3b, whereas the experimental detuning will be in between that situation and the detuning denoted by the diamond in the same figures. This means that although the total width of the miniband will be fixed, the relative position of the middle transition between the outer transitions of each miniband (which we denote α and which will be close to 0.5) depends on the specific middle dot detuning. To overlay the simulation results on the experimental data, we used values of $\alpha = (0.5, 0.6, 0.65, 0.6)$ for the four minibands, respectively. Finally, Extended Data Table 2 gives an overview of the width of the fourth miniband at different tunnel couplings, as Fig. 3b in the main text only plots the data along the ϵ_3 direction. It can be seen that the theory compares well with the experiment along all three directions, which further corroborates the consistency of our measurements.

Data availability. Source data for both main text figures and Extended Data figures are provided with the paper. Raw data and analysis files supporting the findings of this study are available from https://doi.org/10.5281/zenodo.546675.

34. Barthel, C. *et al.* Fast sensing of double-dot charge arrangement and spin state with a radio-frequency sensor quantum dot. *Phys. Rev. B* **81,** 161308 (2010).
35. Colless, J. I. *et al.* Dispersive readout of a few-electron double quantum dot with fast rf gate sensors. *Phys. Rev. Lett.* **110,** 046805 (2013).
36. Van der Wiel, W. G. *et al.* Electron transport through double quantum dots. *Rev. Mod. Phys.* **75,** 1–22 (2002).
37. DiCarlo, L. *et al.* Differential charge sensing and charge delocalization in a tunable double quantum dot. *Phys. Rev. Lett.* **92,** 226801 (2004).

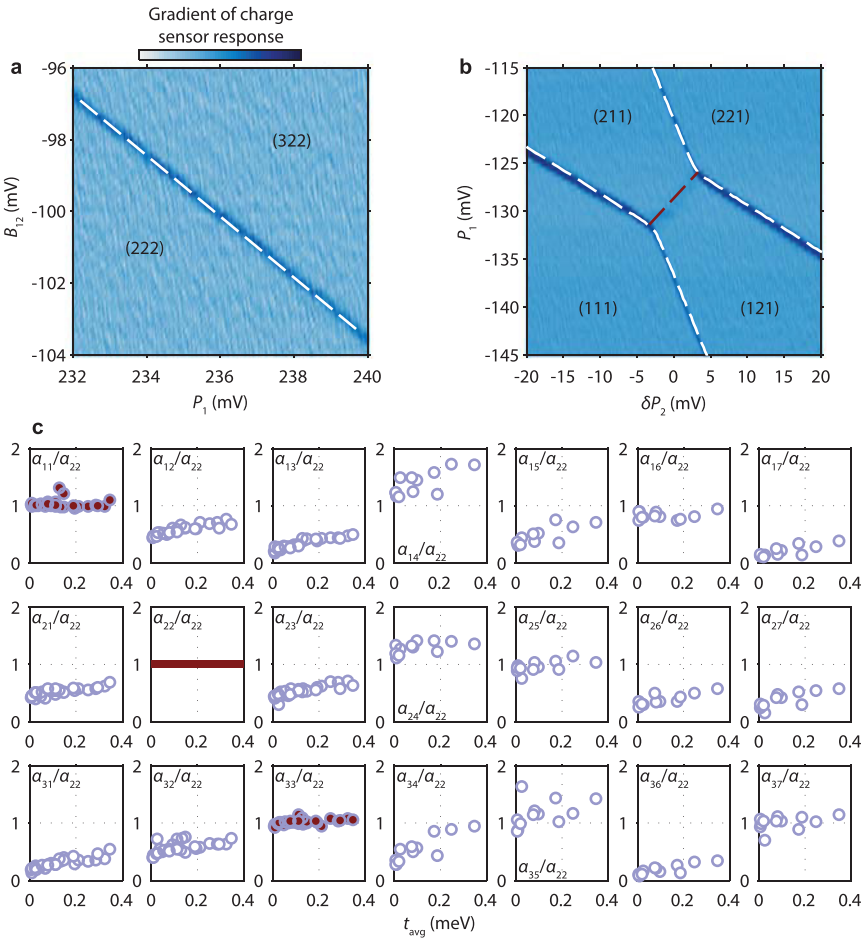

Extended Data Figure 1 | Gate-to-dot cross-talk. a, Cross-talk measurement of gates P_1 and B_{12} on the left dot detuning. (See Fig. 1 for details of the triple-quantum-dot array and associated gates.) The slope of the charge transition (fit in white) yields the relative effect ($\delta B_{12}/\delta P_1 = -\alpha_{11}/\alpha_{14}$) of the two gates on the single-particle energy offset ϵ_1 of the leftmost dot. Note also the non-zero background in charge sensor response we find in experiments, which is due to a direct coupling between the swept gate voltages and the sensing dot conductivity. Text in brackets denotes electron filling. **b**, Charge stability diagram showing the anti-crossing (white) and polarization line (red) between the left and middle dot, yielding the relative effect $\alpha_{11} = \alpha_{21} + [(\delta P_2/\delta P_1)(\alpha_{22} - \alpha_{12})]$ of the two plunger gates (P_1 and P_2) on their respective dots. Automated edge finding and fitting procedures are outlined in Methods. **c**, Measured matrix elements α_{ij}/α_{22} (top left of each panel) as a function of tunnel coupling, t_{avg}. No visual distinction is made between the measured matrix elements at different electron filling. No error bars are shown, as the small uncertainty in the slope fits yields errors smaller than marker size. Note that $\alpha_{22}/\alpha_{22} = 1$ is shown as a line and α_{ii}/α_{22} values as red-filled circles, indicating that they derive from the slopes of polarization lines, such as the one shown in red in **b**.

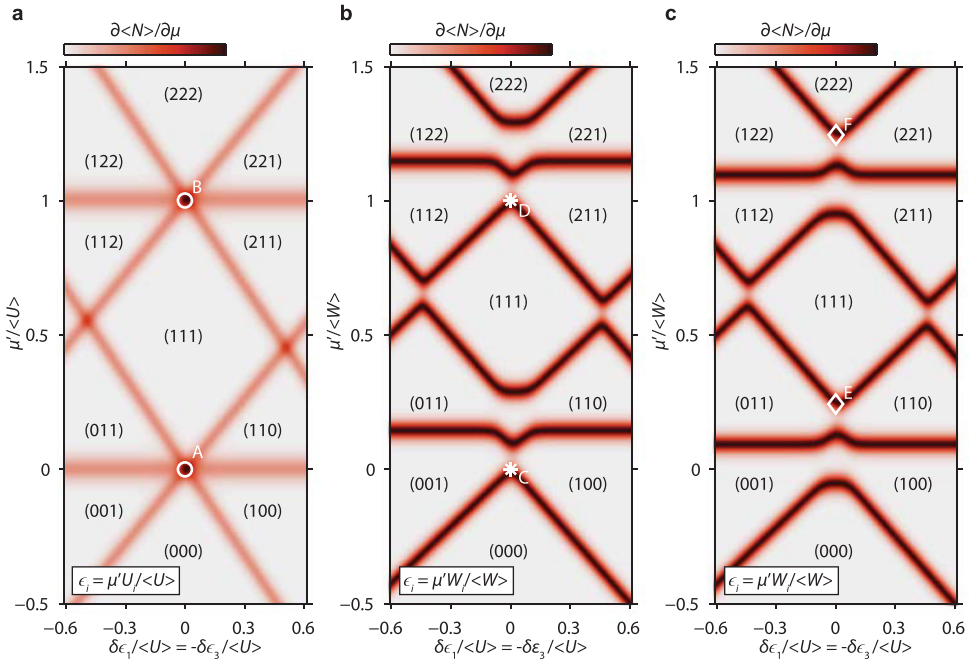

Extended Data Figure 2 | Simulated classical charge addition spectra. **a**–**c**, Simulated charge addition spectra (see Methods for details and nomenclature) for a triple quantum dot at zero tunnel coupling, $U_2 = 1.05U_1 = 0.95U_3$ and up to two particles per dot, connected to a reservoir at $\mu = 0$ and $k_B T = 0.02U$ (>10 times larger than for the experiments described in the main text), with $V_{ij} = 0$ and $\delta_i = 0$ (**a**) or with $V_{12} = V_{12} = 2V_{13} = 0.2U$ and $\delta_i = 0$ (**b**) or $\delta_1 = \delta_3 = 0$ and $\delta_2 = U/15$ (**c**). $N = \sum_i n_i$ denotes total electron filling, $W_i = U_i + \sum_{j \neq i} V_{ij}$ the sum of local interactions. States are denoted by charge occupation (n_1 n_2 n_3) and specific degeneracy points A–F are referred to in Methods. The relation between ϵ_i and μ' specified in the boxes at lower left applies to the vertical line at zero (horizontal) detuning.

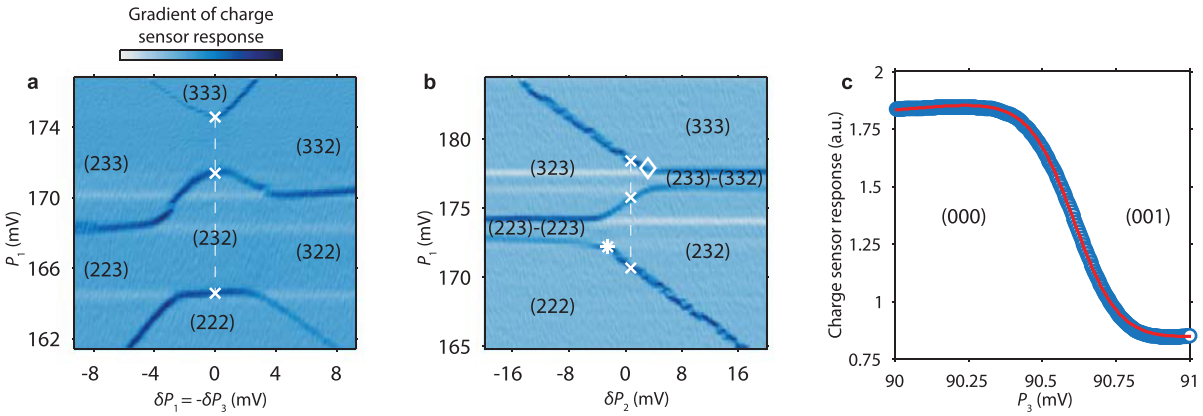

Extended Data Figure 3 | Miniband width and electron temperature. **a**, Measured charge stability diagrams of the (222)–(333) miniband as a function of homogeneous filling (only P_1 values are shown) and offset in the outer two dot energies by changing P_1 and P_3 in opposite directions, akin to the simulations of Extended Data Fig. 2c. For crosses and dashed line, see **b**. **b**, Similar measurement as a function of the offset in the middle dot energy, controlled by P_2. The P_1 values are somewhat different from those in **a** because these measurements were taken at slightly different tunnel coupling tunings. The white diamond and asterisk indicate (roughly) the position of the same degeneracy points as shown in Extended Data Fig. 2. **c**, Broadening of a charge addition line (blue) due to the finite temperature of the (rightmost) Fermi reservoir. A Fermi–Dirac fit of the transition is shown in red, which yields an effective reservoir temperature of 72(1) mK.

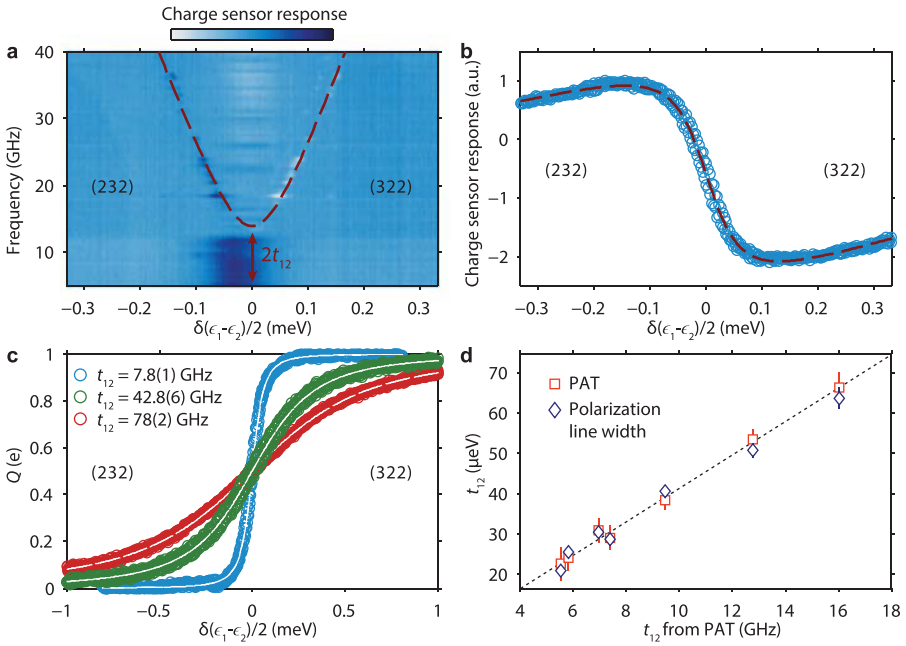

Extended Data Figure 4 | Determining lever arm and tunnel coupling. **a**, Example of a photon assisted tunnelling (PAT) measurement, which at low tunnel couplings is the measurement method of choice for both lever arm and tunnel coupling. Plotted is the difference in charge sensor response between applying a microwave excitation (y axis) or not as a function of detuning (x axis). Dashed red line is a fit to the hybridized charge state spectrum of the double dot[24]. The energy difference between bonding and antibonding states yields the minimum in frequency ($2t_{ij}$, here for dots 1 and 2) and the slope away from the transition gives the lever arm between detuning voltages applied to the gates and single-particle energy difference change between the two dots. The need to generate AC excitations and transmit them without severe losses through coaxial cables in the dilution refrigerator set-up, however, limits the maximum tunnel frequency we can accurately determine with this method to roughly 20 GHz (83 μeV). **b**, Example of a polarization line width measurement (blue circles), with fit in red. As an alternative to PAT, one can determine the tunnel coupling by assessing the width of the polarization line[37]. The excess charge (say on the left dot) transition is broadened both by an effective electron temperature and by the tunnel coupling. Charge sensor response is however not a direct measurement of excess charge. Not only does there exist a finite cross-talk between the gate voltages and the charge sensor response that leads to a finite slope away from the transition, we also typically find a back-effect of the excess charge on the sensing dot, leading to a different slope on either side of the transition. We fit the data with the following equation, taking this back-effect into account to first order in excess charge: $V(\epsilon) = V_0 + \delta V\, Q(\epsilon) + \left[\left.\frac{\delta V}{\delta \epsilon}\right|_{Q=0} + \left(\left.\frac{\delta V}{\delta \epsilon}\right|_{Q=1} - \left.\frac{\delta V}{\delta \epsilon}\right|_{Q=0}\right) Q(\epsilon)\right]\epsilon$, where $V(\epsilon)$ is the charge sensor response as a function of the detuning $\epsilon = \delta(\epsilon_i - \epsilon_j)$ away from to the transition and V_0, δV and $\frac{\delta V}{\delta \epsilon}$ are the background signal, sensitivity and gate–sensor coupling, respectively. Note that ϵ is a linear combination of the swept gate voltages, taking the relevant cross-capacitances and the lever arm into account. Excess charge on the left dot is described by $Q(\epsilon) = \frac{1}{2}\left(1 + \frac{\epsilon}{\Omega}\tanh\left(\frac{\Omega}{2k_B T_e}\right)\right)$, with $\Omega = \sqrt{\epsilon^2 + 4t_{ij}^2}$ and effective temperature $k_B T_e \approx 6.5\,\mu eV$ (1.6 GHz). **c**, Excess charge as function of detuning for three different tunnel couplings, showing that this characterization method works up to tunnel couplings that are several times higher than those measurable by PAT. **d**, Comparison of PAT and polarization line width measurements. The data are well explained by assuming a constant lever arm $\alpha_{22} = 83(1)\,\mu eV$ per mV between gate P_2 and the middle dot. Text in brackets denote relevant charge states; error bars are 1σ fit uncertainties.

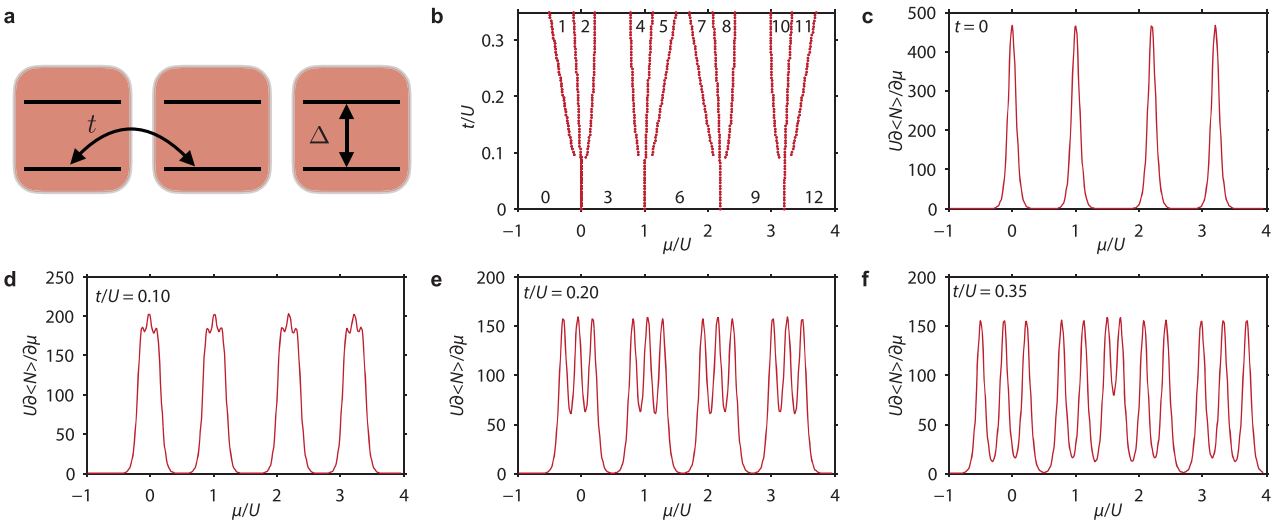

Extended Data Figure 5 | Simulations of collective Coulomb blockade for the simplified Hubbard model. a, Cartoon diagram of a triple-dot system, which is a simplified version of the model used to describe the experiments in the main text. Specifically, we have set a uniform tunnel coupling t and Hubbard U (not shown), while ignoring the inter-site Coulomb interaction term V_{ij}. We describe two levels per dot with a level splitting Δ that separates the single-particle energies of the first and second orbital. Each energy level is doubly degenerate owing to the spin degrees of freedom. **b**, Peaks in the electron addition spectrum for the triple-dot system in **a**. It is known that the classical Coulomb blockade effect arises purely from the charging effects of the quantum dots. When electron tunnelling between quantum dots is allowed, however, quantum fluctuations compete with the classical charging effects and give rise to a rich phase diagram, which is known as collective Coulomb blockade[20]. The metal–insulator transition in such a system is best captured by the charge addition spectrum, which is precisely what we measure in the experiment (Fig. 3b). The numbers in **b** (at top and bottom of the panel) indicate the average electron numbers in the system when the chemical potential μ resides at the respective gap. Here we use $\Delta/U = 0.2$, and $k_BT/U = 0.04$ (>20 times larger than for the experiments described in the main text). **c**–**f**, Line cuts for the addition spectrum in **b** at different values of t/U (shown at top left of each panel). As discussed in the main text, there will be three different regimes in this phase diagram: at weak tunnel couplings the quantum dot states split into minibands but the isolated Coulomb blockade of each individual dot is preserved; at intermediate tunnel couplings the Coulomb blockade of individual dots is lost, but the gap between minibands remains open; finally, in the large tunnel coupling limit the gap between minibands can become comparable to temperature, and the system will be in a metallic state. The same can be seen in these line cuts. At $t = 0$ we can see that there are four critical chemical potentials μ at which electrons can be added to the triple dot. For the present model, these four peaks occur at $\mu = 0$, U, $2U + \Delta$, and $3U + \Delta$, respectively. Each peak is triply degenerate, as the energy cost of adding electrons to any of the three dots is identical. For non-zero but small tunnel couplings (**d**, **e**) each triply degenerate peak at $t = 0$ starts to split into a miniband, indicating the breakdown of Coulomb blockade in each dot. However, different minibands are still separated by gaps that arise from a collective origin, reminiscent of the energy gap in a Mott insulator. Finally, at sufficiently high tunnel couplings we find non-zero $\frac{\partial\langle N\rangle}{\partial\mu}$ at the middle gap (**f**), indicating that Coulomb blockade is completely overwhelmed by temperature.

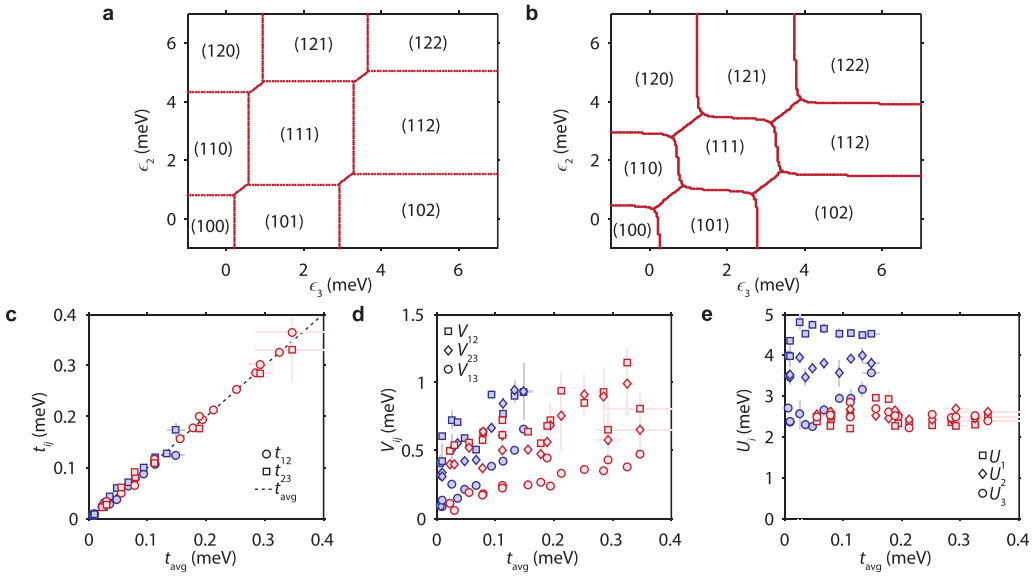

Extended Data Figure 6 | Characterizing model parameters. a, Simulated charge stability diagram for a triple-dot system with parameters $t = 0.006$, $U_1 = 3.98$, $U_2 = 3.48$, $U_3 = 2.70$, $V_{12} = 0.41$, $V_{23} = 0.35$, $V_{13} = 0.11$ (all energies in meV). As described in Methods, the eigenstates can be obtained exactly in the $t = 0$ limit, as the eigenstates of the triple-dot system can be represented simply by the charge states $(n_1\ n_2\ n_3)$. In this regime, one can show that on the ϵ_2–ϵ_3 plane the border between the (111)/(112) region and the border between the (111)/(110) region are exactly separated by an energy of U_3. Similarly, the border between the (111)/(121) region and the border between the (111)/(101) region are separated by an energy of U_2. In the presence of a non-zero but small tunnel coupling as is the case here, we expect that such an estimate is still reasonable. Now that the tunnel coupling is non-zero, the ground state of the system is no longer an exact charge state $(n_1\ n_2\ n_3)$, but generally a superposition of different charge states. To retain a connection to the $t = 0$ limit, we keep labelling sections of the charge stability as $(n_1\ n_2\ n_3)$, but with the distinction in mind that $(n_1\ n_2\ n_3)$ no longer denotes the exact ground state, but instead the charge state with the largest weight in the actual ground state. As a check, we can determine the values of U_2 and U_3 from the simulated charge stability diagram using the method described above and find that $U_2 = 3.44$ meV and $U_3 = 2.71$ meV, respectively, which is reasonably close to the corresponding model parameters. Because the data in Fig. 2c are taken at $t/U = 0.002$, we can thus trust the extracted U. **b**, Charge stability diagram for a triple-dot system with parameters $t = 0.17$, $U_1 = 2.92$, $U_2 = 2.39$, $U_3 = 2.53$, $V_{12} = 0.55$, $V_{23} = 0.47$, $V_{13} = 0.27$ (all energies in meV). We find that the structure of the charge stability diagram remains qualitatively the same as that in **a**, and if we again extract the values of U_2 and U_3 using the same method, we find that $U_2 = 2.48$ meV and $U_3 = 2.56$ meV, which still agrees reasonably well with the original model parameters. Granted, at sufficiently large t/U the structure of the charge stability diagram will change drastically, and the present method to extract model parameters is bound to fail. However, as we never enter those regimes, our fitting method serves the purpose of this experiment. **c–e**, Calibrated tunnel couplings (**c**) and measured inter-site Coulomb (**d**) and on-site Coulomb (**e**) terms at calibrated values of the average tunnel coupling, corresponding to the experimental parameter space plot shown in Fig. 3b. Plotting symbols are defined in each key; blue shows data from the first subband from 0 to 6 electrons, red shows data from the second subband from 6 to 12 electrons. Error bars are 1σ fit uncertainties.

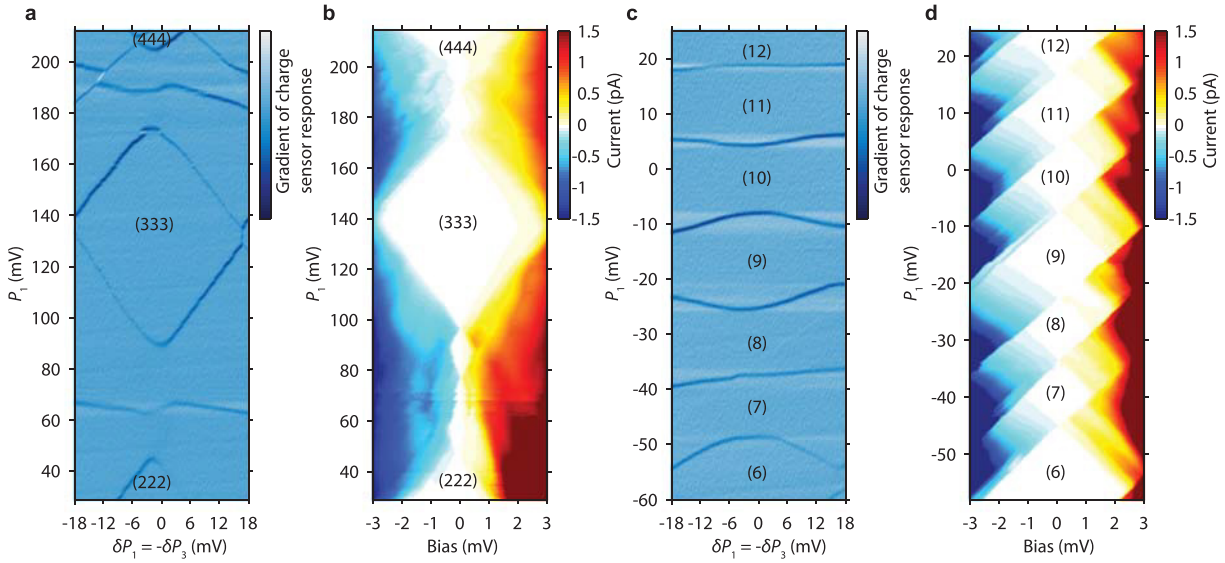

Extended Data Figure 7 | Isolated versus collective Coulomb blockade in charge and transport. a–d, Charge stability diagrams (**a** and **c**) and transport through the array (**b** and **d**), at low (**a** and **b**) and high (**c** and **d**) tunnel coupling. Panels **a** and **c** show charge stability diagram around the (333) regime in the low (**a**) and high (**c**) tunnel coupling regimes, using a combination of all seven gates (only P_1 values are shown) that change the local fillings equally. To further investigate the distinct phases, we focus on the regime with around nine electrons in total, corresponding to half-filling of the second band, and look at both charge sensing and transport. In the localized phase ($t/U < 0.02$ in **a**), the charge stability diagram shows transition lines following three distinct, well-defined directions, corresponding to the filling of the separate lithographically defined dots. In the delocalized phase ($t/U > 0.15$ in **c**), this distinct nature is all but lost, highlighting the incipient formation of a large single dot. The same effect can also be seen in transport measurements, as we observe Coulomb diamond sizes as a function of filling. **b**, Transport through the array following the zero-detuning line of Fig. 2b as a function of applied bias (60% on leftmost and 40% on bottom right reservoir). In the (333) state, this applied bias has to overcome the local (strong) Coulomb repulsion in order for current to flow, similar to a Mott insulator whose Fermi energy resides inside the gap. Adjacent Coulomb diamonds correspond to a Fermi-level inside the miniband and are significantly smaller, allowing current to flow at much smaller bias voltages. **d**, Similar data in the high tunnel coupling regime. Whereas the individual nature of the dots is all but gone, global (weaker) Coulomb repulsion still prohibits transport at small bias, as expected for the collective Coulomb blockade phase. The notion of a large gap at half-filling is gone, and it is only the charging energy of the entire system that prohibits transport occurring, regardless of filling. The dots are in collective Coulomb blockade, and its transport characteristics are similar to that of a small, metallic island.

Extended Data Table 1 | Example of simulated transition points

Transition	6 to 7	7 to 8	8 to 9	9 to 10	10 to 11	11 to 12	Width 9 to 12	(Exp.)
ε_1	6.3800	7.1280	8.0460	9.7800	10.5620	11.5140	1.7340	1.6671
ε_2	7.4600	8.3664	9.4788	11.5800	12.5276	13.6812	2.1012	1.9082
ε_3	6.6600	7.4432	8.4044	10.2200	11.0388	12.0356	1.8156	1.7391
μ	6.6200	8.9800	8.9800	10.1000	11.0200	13.2600	3.1600	-

Shown are transition points for a triple-dot system with parameters $t = 0.29$, $U_1 = 2.26$, $U_2 = 2.70$, $U_3 = 2.48$, $V_{12} = 0.65$, $V_{23} = 0.57$, $V_{13} = 0.43$ (all in meV). The column headings $N_1 \rightarrow N_2$ indicate that the data for each column are for the transition from a total of N_1 particles to N_2 particles. ϵ_i ($i = 1, 2, 3$) are the 'local' chemical potentials on each dot, while μ is the 'uniform' chemical potential. The last two columns compare the simulated and experimental (Exp.) total width of the fourth miniband. All energies are in meV.

Extended Data Table 2 | Experimental and theoretical miniband widths

t	ε_1 (Th.)	ε_1 (Exp.)	ε_2 (Th.)	ε_2 (Exp.)	ε_3 (Th.)	ε_3 (Exp.)
0.077	1.0032	1.0110	1.1616	1.1732	1.0164	0.9941
0.1117	1.1552	1.1150	1.4288	1.5409	1.2312	1.3710
0.1880	1.5824	1.5609	1.8216	1.7059	1.6192	1.5274
0.2930	1.7340	1.6671	2.1012	1.9082	1.8156	1.7391
0.3480	2.0352	1.9609	2.3532	2.1396	1.9080	1.9596

Comparison of the experimental (Exp.) and theoretical (Th.) width of the fourth miniband in Fig. 3b at five calibrated values of the tunnel coupling, t. Theoretical widths take the interaction energies measured at the specific tunnel coupling values into account (see Extended Data Fig. 6). All energies are in meV.